Study of variability of 1D site response in Kushiro10 from records and an analytical model
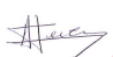
Work Package #4 "Site response"

AUTHORS		REVIEW		APPROVAL	
Name	Date	Name	Date	Name	Date
Stefano CHERUBINI Irmela ZENTNER	2020/03/15	Signature numérique de Alain PECKER DN : cn=Alain PECKER, o=AP Consultant, ou, email=alain.pecker@orange.fr, c=FR Date : 2021.01.17 20:37:46 +01'00' Christophe Martin	2021/02/19	Emmanuel Viallet Public access ⦿ SIGMA-2 restricted ○	2021/12/12

Stefano CHERUBINI, Irmela ZENTNER – Study of the variability of 1D site response in Kushiro10 from records and an analytical model - *SIGMA2-2020-D4-048*

Document history

DATE	VERSION	COMMENTS
2021/01/12	*0*	*Reviewers' comments taken into account*

Executive summary

The 1D site response is still nowadays the most largely diffused technique in geotechnical earthquake engineering in order to evaluate site effects. In the paper "A taxonomy of site response complexity" (Thompson, et al., 2012), using 100 Kiban–Kyoshin network (KiK-net) surface–downhole pairs in Japan, Thomson develops taxonomic rules that separate downhole seismic arrays into four categories based on inter-event variability and the complexity of the wave propagation model required to match ground motions from small events. Now, even if, according to this analysis, the Kushiro10 site is a 1D linear elastic vertical propagation site, a large variability in peaks and eigen frequencies has been remarked by plotting the empirical transfer functions (ETFs). The final goal of this work is to quantify the empirical variability observed on 1D ETF obtained from vertical arrays and the proxies leading to the highest variability, in order to improve the reliability of 1D numerical quantification of site effects.

In this work, a qualitative analysis of the Kushiro10 site KiK-net data has been accomplished. This analysis has allowed to understand the main variability sources in the transfer functions when considering the 1D vertical propagation site hypothesis. With the data analysis, two main variability sources have been identified: (i) The incidence angle that has a strong impact on the variability of the transfer functions; (ii) The PGA values that have a medium impact on the variability of the transfer functions. Also, an analysis of the damping has been done and it showed that the elastic attenuation could be underestimated. These results suggest that the 1D propagation hypothesis is maybe too strong for the Kushiro10 site. Indeed, even if the site morphology suggests a 1D stratigraphy, a 1D site response model seems to be not enhanced enough to take into account the variability provided by the seismic signals (in particular the incidence angle) and by the damping.

Furthermore, in a future analysis, it would be highly interesting to repeat this kind of analysis for other sites and compare the results to Kushiro. In perspective, a 2D model can be considered to complete this study in order to better investigate this first results in terms of variability. A comparison between the 1D site response and the 2D site response could be a good method to test the impact of the incidence angle on the site response.

1.   Introduction

The 1D site response is still nowadays the most largely diffused technique in geotechnical earthquake engineering in order to evaluate site effects. Those site effects are spatially variable depending on the local geomorphology and mechanical properties of the soil and this variability is accentuated when the seismic response is non-linear ((Seed & Idriss, 1969), (Vucetic & Dobry, 1988), (Ishibashi & Zhang, 1993), (Yu, et al., 1993), (Elgamal, et al., 1995), (Zeghal, et al., 1995), (Gunturi, et al., 1998), (Bonilla, et al., 2005), (Amorosi, et al., 2016)).

In the paper "A taxonomy of site response complexity" (Thompson, et al., 2012), using 100 Kiban–Kyoshin network (KiK-net) surface–downhole pairs in Japan, Thomson develops taxonomic rules that separate downhole seismic arrays into four categories based on inter-event variability and the complexity of the wave propagation model required to match ground motions from small events. Thompson evaluates the accuracy of site response models by comparing theoretical transfer functions (TTFs) to empirical transfer functions (ETFs). The most common assumptions for computing a TTF (SH1D site response model) include: (1) the medium is assumed to consist of laterally constant layers overlying a non-attenuating half-space; (2) wave-fronts are assumed to be planar; (3) only the horizontally polarized component of the S wave (the SH wave) is modeled; (4) damping is assumed to be frequency-independent.

Thus, all sites are separated into four distinct categories:

- 1st category: sites that have low inter-event variability and that are a good fit to the SH1D site response model. These sites are ideal for calibration and validation of one-dimensional constitutive models;
- 2nd category: sites that have low inter-event variability and that are a poor fit to the SH1D site response model. These sites are appropriate for nonlinear modeling but care must be taken to identify the source of the misfit (e.g., soil heterogeneity, profile recalibration/optimization).
- 3rd category: sites that have high inter-event variability and that are a good fit to the SH1D site response model and thus they are not likely to be informative for nonlinear constitutive models unless path and source effects can be accounted for;
- 4th category: sites that have high inter-event variability and that are a poor fit to the SH1D site response model. These sites are difficult to interpret because we would expect that if the inter-event variability is large, the fit to the SH1D should be poor.

Now, even if, according to this analysis, the Kushiro10 site is in the first category, a large variability in peaks and eigen frequencies has been remarked by plotting the ETFs. Indeed, the fact that only one site is considered cannot lead to a generic conclusion. We decided to work with this particular site as it is a well-known site from the Prenolin benchmark (Régnier, et al., 2018) (the Kushiro10 site has been the object of an extensive site characterization), but we intend to continue the analysis on others sites. The final goal of this work is to quantify the empirical variability observed on 1D ETF obtained from vertical arrays and the proxies leading to the highest variability, in order to improve the reliability of 1D numerical quantification of site effects.

This document is organised as follows:

- In chapter 2, the Kushiro10 site is presented. In particular, a focus on KiK-net data and on the mechanical and geometrical characteristic of the site is made. Finally, the pre-treatment of all recorded data and the relative transfer functions is presented, with a first quantification of the variability;
- In chapter 3, the variability is analysed according to some fundamental parameters:

  - The peak ground acceleration (PGA) of all time histories;
  - The Azimuth between site and seismic source
  - The incidence angle of the seismic signal at the bedrock;
  - The experimentally estimated damping of the Kushiro10 soil column from the recordings.

  A summary of the data analysis is made, by classifying the variability sources and their impact on the transfer functions.
- Finally, some conclusions and perspectives are provided.

This work is part of Work Package 4 of the Sigma2 project.

2.   Site choice and KiK-Net Data pre-processing

In this chapter, the site and the reasons for which it has been chosen are presented. Moreover, all the pre-processing analyses on the seismic signals of the site are described.

2.1.   Kushiro site

The site that has been chosen is in Kushiro, in the Hokkaido region (Japan). In Figure 1, the geographical localization is shown.
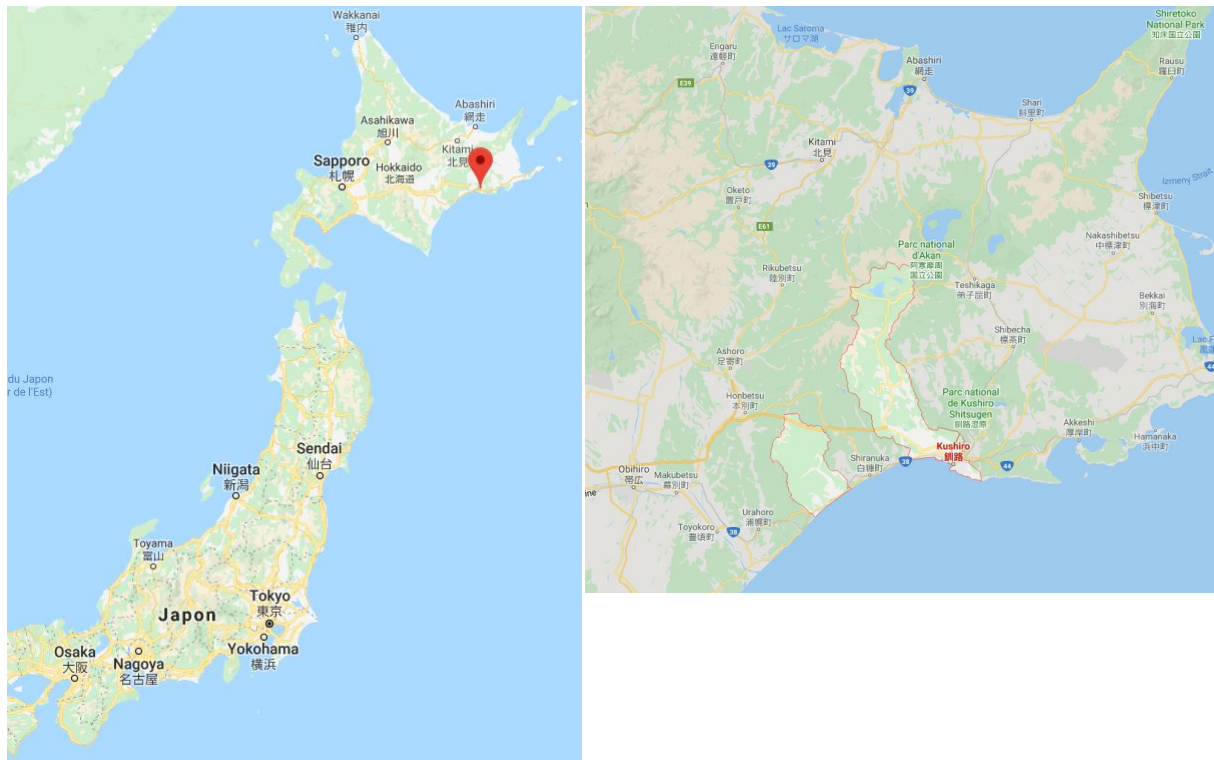

Figure 1: Geographical localization of the site

This site has been chosen on the basis of the following requirements (Régnier, et al., 2018):

- Availability of both strong and weak motion recordings;
- Plausibility of 1D wave propagation assumption.

To fulfill the first requirement, at least two earthquakes with PGA higher than $50\ cm/s^2$ have to be in the list of the available recordings at the downhole sensor. The Kushiro10 site satisfies this condition. For the second requirement, the 1D wave propagation hypothesis can be assumed according to the criteria proposed by (Thompson, et al., 2012). In the (Thompson, et al., 2012), a site response classification scheme for surface-downhole strong motion arrays is proposed. The accuracy of the site response is evaluated by comparing the theoretical transfer functions (TTFs) to the empirical transfer functions (ETFs). In particular, the most common assumptions for computing TTF include:

- The medium is assumed to consist of laterally constant layers overlying a non-attenuating half-space;
- Wave fronts are assumed to be planar;
- Only the horizontally polarized component of the S-wave (the SH wave) is modeled;

- Damping is assumed to be frequency independent.

All the assumptions mentioned can be included in the SH1D site response model. (Thompson, et al., 2012) quantify the inter-event variability of the ETF as the median of the maximum likelihood estimate for the standard deviation of the ETFs between the first and fourth peaks of the SH1D transfer functions (σ_i). With these criteria, the Kushiro10 site has been identified as a site that has a low σ_i and that is a good fit to SH1D. It's ideal for the calibration and validation of a one-dimensional constitutive model.

2.2. Mechanical properties of the soil column

The Kushiro10 site is a deep sedimentary site with 40 m of low-velocity soil layers. The site is located on the lower plateaus with about 30 m in elevation along the right bank (southern) side of the upper Anebetsu River. The soil column consists of recent Younger Volcanic Ash deposits down to 5 m in depth, followed by volcanic and Tuffaceous sand until 40 m and underlain by an alternation of sandstone and shale (Régnier, et al., 2018).

In Table 1, the mechanical properties of the soil column of Kushiro10 are shown:

- Z is the depth of the soil layer;
- V_S is the shear wave velocity of the soil layer;
- V_P is the compressional wave velocity of the soil layer;
- ρ is the density of the soil layer;
- Q_S is the elastic attenuation;
- ξ is the elastic damping ratio.

Z (m)	V_S (m/s)	V_P (m/s)	ρ (kg/m³)	Q_S	ξ
6	140	1520	1800	25	0.02
11	180	1650	1800	25	0.02
15	230	1650	1500	25	0.02
20	300	1650	1500	25	0.02
24	250	1650	1600	25	0.02
28	370	1650	1600	25	0.02
35	270	1650	1800	35	0.0142
39	460	1650	1800	25	0.02
44	750	1800	2500	75	0.0066
84	1400	3400	2500	140	0.0035
255	2400	5900	2500	240	0.0020

Table 1: Mechanical properties of the soil column of Kushiro 10

Some details on how the mechanical parameters have been obtained are reported here from (Régnier, et al., 2018).

Measurements performed. To obtain the linear and NL soil parameters, in situ measurements and multiple laboratory measurements were conducted on disturbed and undisturbed soil samples. The in situ measurements were subcontracted to Oyo Company and consisted in (1) boring investigation to determine soil stratigraphy and to perform the soil sampling. The diameter of the borehole was 116 mm up to a depth where triple-tube samplings were used (for sandy soil or relatively stiff clayey soil) then 86 mm; (2) undisturbed soil samples (80 cm long) were collected using the thin-wall sampler for the soft clay soil and using the tripled-tube samplers for the sand and stiffer clayey soil; (3) standard penetration tests; (4) PS logging by suspension method; and (5) multiple multichannel analysis of surface waves (MASW) at the investigated sites to characterize the spatial variability of the underground structure at shallow depth, together with single-point ambient vibrations recordings. The laboratory soil tests were conducted on disturbed and undisturbed soil samples. The tests on disturbed samples have been useful to determine physical characteristics such as particle size distribution, liquid, and Atterberg limits. The tests on undisturbed soil samples aim at defining the density and to perform a wide range of laboratory tests such as undrained and drained triaxial compressional test, oedometer tests by incremental loading, cyclic undrained and drained triaxial compression test (undrained for investigating the liquefaction potential) and, for rock samples, unconfined compressional tests. The methods used to perform the laboratory tests are defined by Japanese normative specifications. For each borehole, the number of undisturbed soil samples was defined according to the expected soil stratigraphy (on the basis of pre-existing KiK-net information), to ensure at least one sample in each homogeneous soil unit.

Elastic and Viscoelastic Properties. For the elastic properties, several methods were used to determine the soil parameters. The PS logging has been used to obtain the V_S profile and then the earthquake recordings has been used to adjust it. As shown in the Figure 2, the V_S profile was adjusted to improve the fit between the fundamental resonance frequency recorded and predicted for the Kushiro10 site. The initial V_S profile was based on the PSlogging investigation down to 50 m depth; beyond this depth, the values of the V_S coming from the KiK-net database have been considered, where the PS-logging method was also used. In this project, it was decided to adjust the linear transfer function from Thomson–Haskell predictions to the instrumental observations of surface–borehole spectral ratios, to ensure that the discrepancies between the prediction and the observations during the benchmark were associated with NL soil behavior, and not to other causes. To adjust the numerical linear transfer function to the observation, the V_S profile coming from KiKnet for which no information was available on the measurement has been modified.

The Poisson coefficient (v) was computed using the PS logging and rounded. To ensure consistency between the values of V_S, V_P, and v, the V_P parameter was obtained from V_S and the rounded v. The density was obtained from the undisturbed soil sample and the low-strain attenuation was deduced from the undrained cyclic triaxial test, and, when not available, using the rule of thumb ($Q_S /V_S=10$) (Olsen, et al., 2003).

Please remark that the Poisson coefficient is not furnished in the PRENOLIN paper, but we computed this parameter from the Vs and Vp values.

The Figure 2, from (Régnier, et al., 2018), shows the ETFs in grey and two TTFs: the dashed dark line is the TTF provided by the Vs profile available from Kik-Net and the red line is the TTF obtained from the Vs profile given by the benchmark organizers. As one can see, the frequency modes are reasonably well captured, although the amplitude of the TTF is higher than the ETFs. No 2D model was performed during the benchmark exercise.
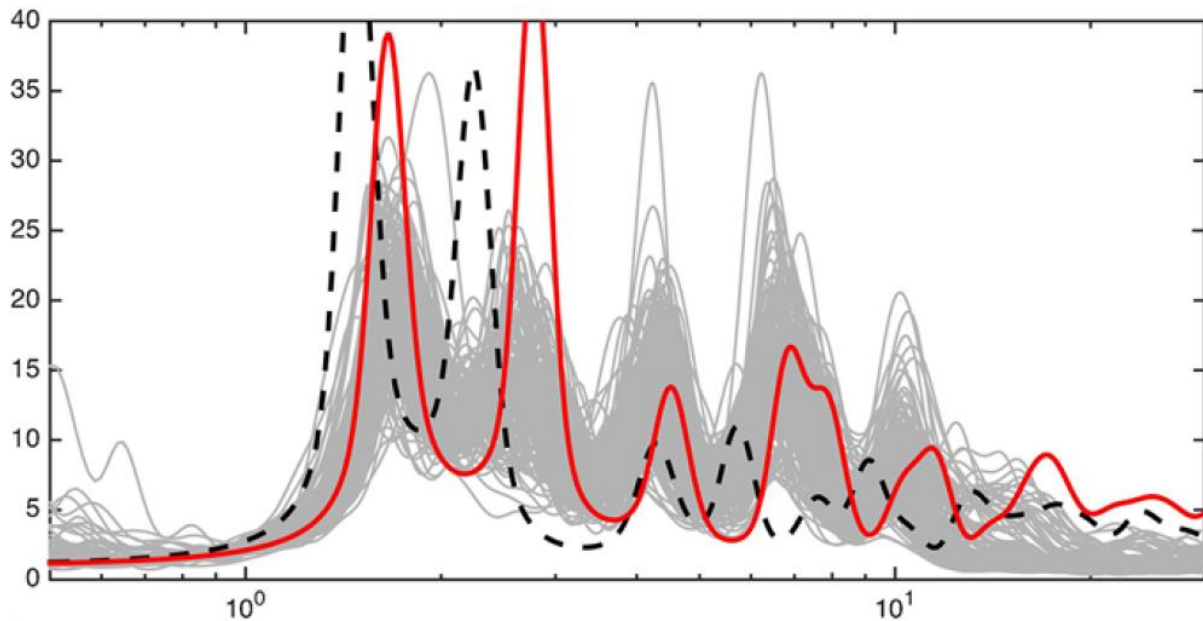

Figure 2 : Borehole transfer functions on Kushiro10 site

2.3.   KiK-net database

KiK-net (Kiban Kyoshin network) is a strong-motion seismograph network, which consists of pairs of seismographs installed in a borehole together with high sensitivity seismographs (Hi-net) as well as on the ground surface, deployed at approximately 700 locations nationwide. NIED constructed KiK-net under the plan 'Fundamental Survey and Observation for Earthquake Research' directed by 'the Headquarters for Earthquake Research Promotion'.

The strong-motion data recorded by KiK-net are immediately transmitted to the data management center of NIED in Tsukuba. The observed strong-motion data are widely available to the public through the internet from the web site (NIED, 2019).

For the Kushiro10 site, more than 600 time histories recorded between 2001 and 2015 are available. For each record, two seismic signals have been captured in two distinct points (borehole and surface). For each signal, three components are available: the vertical component "Up/Down" (UD) and two horizontal components "East/West" (EW) and "North/South" (NS). The KiK-net Database for the Kushiro site consists of more than 3000 acceleration time-histories.

All the information for the Kushiro site records (in the ASCII format) are:

-   Event origin time;
-   Event latitude;
-   Event longitude;
-   Event depth (km);

- Magnitude;

- Site code;

- Site latitude;

- Site longitude;

- Site altitude;

- Recording start time;

- Sampling frequency (Hz);

- Recording duration time (s);

- Channel number;

- Scale factor (cm/s^2);

- Maximum acceleration (cm/s^2);

- Time of last correction;

- Strong-motion data.

The acceleration time series are obtained by multiplying the strong-motion data by the scale factor. The depth of the downhole sensor is 255 m. In the PRENOLIN benchmark (Régnier, et al., 2018) it has been verified that both surface and downhole sensors are oriented in a similar way. The surface horizontal components have been rotated anticlockwise with a 1° azimuth increment, starting from the original EW orientation, and the correlation coefficient with the downhole EW component has been calculated. Both signals were filtered between 0.1 and 1 Hz. The values obtained suggest that both surface and downhole EW components are mostly oriented parallel to each other, and, even if slight deviations of the order of 7° may occur, it would not significantly impact the soil response functions.

2.4. Data pre-processing

All acceleration time series have been submitted to a pre-progressing process, before applying the Fast Fourier Transform (FFT). In particular, a baseline correction with asymmetric least squares smoothing (Zhang, et al., 2010) has been applied.

After this pre-processing phase, the FFTs of all acceleration time histories have been calculated. Before performing the transfer functions (**the spectral ratio between the surface records and the downhole records**), a Konno-Omachi smoothing (with b = 40 as it is classically fixed) has been applied (Konno & Ohmachi, 1998). One example of the Konno-Omachi smoothing applied to a FAS is shown in Figure 3. Konno and Omachi propose a logarithmic window function expressed as:

$$W_B(f, f_c) = [\sin(\log_{10}(f/f_c)^b)/\log_{10}(f/f_c)^b]^4 \qquad (2.1)$$

where b, f and f_c are a coefficient for band width, frequency and a center frequency, respectively.

The Konno-Omachi smoothing window is calculated for each center frequency of the frequency domain. A different smoothing window for each center frequency has been used. The b parameter is fixed as the default value 40. When the center frequency is 0, the smoothing

window is equal to 1. First, the center frequency is fixed, then the window smoothing on the frequency vector is calculated (N_f is the length of the frequency vector) and a vector of length N_f x1 is obtained. Then, this operation is repeated for each center frequency and a smoothing matrix (N_f x N_f) is obtained. This matrix is applied to the ETF in order to obtain the smoothing function.

Furthermore, an analysis of signal-to-noise ratio has been done by (Regnier, 2013). For more than 75% of the signals, in the frequency amplification range of Kushiro10 (between 1 and 10Hz), the signal-to-noise ratios (SNRs) were high enough (SNR > 3). In Figure 4, where the SNR is not good, a red point is marked.
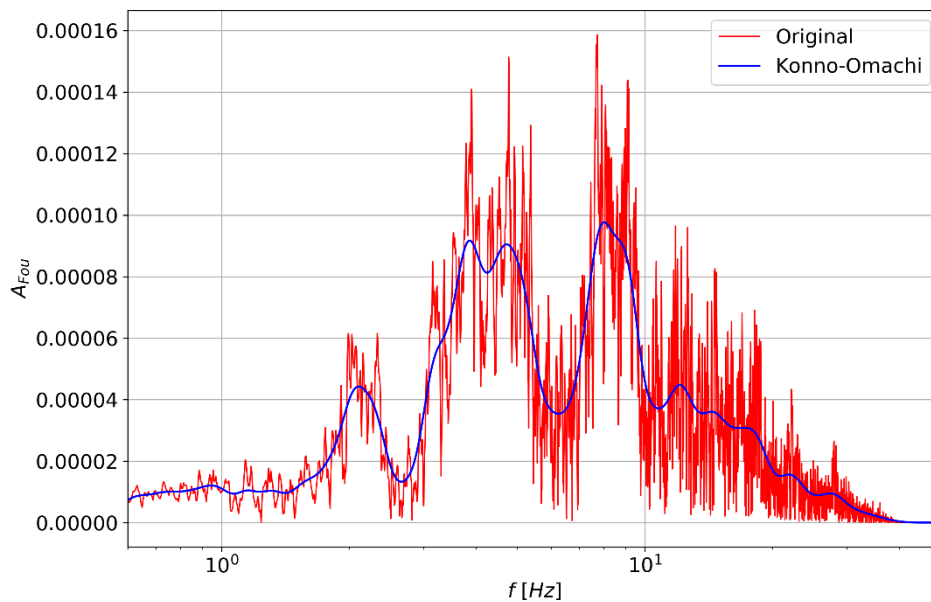
Figure 3 : A Fourier transform of a time history (in red) with its Konno-Omachi smoothing (in blue)
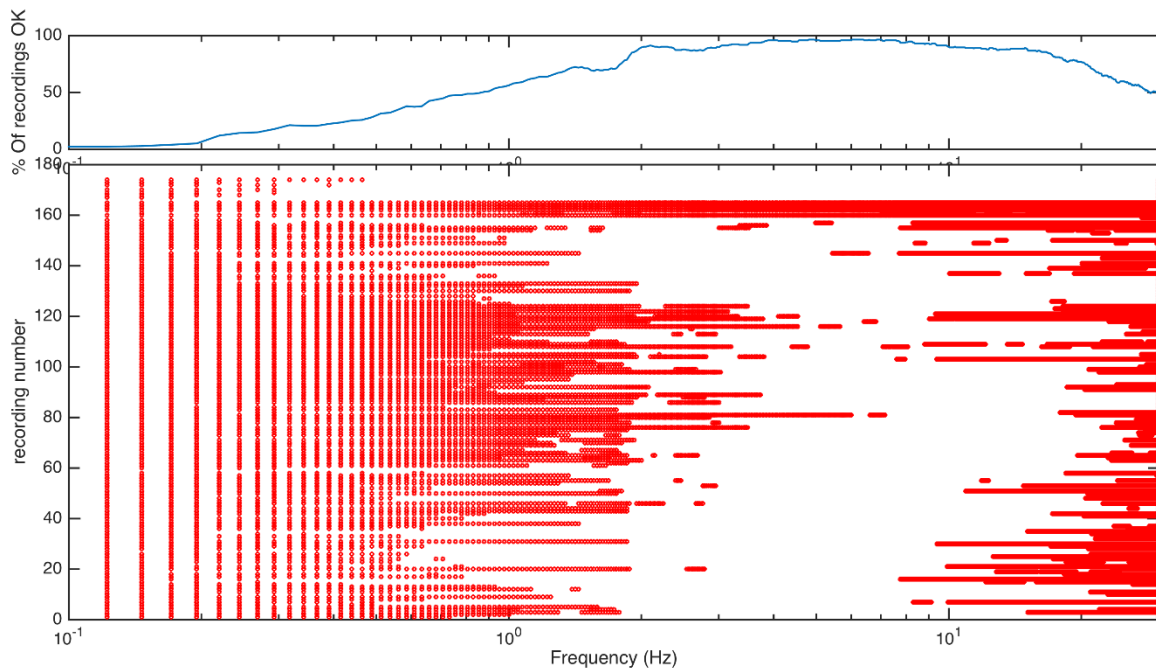
Figure 4 : Analysis of signal-to-noise ratio for Kushiro10 site signals

2.5.   Analysis of transfer functions

In order to analyze the trend of the transfer functions for every time history recorded, all the transfer functions are shown in Figure 5 (for the East-West direction), in Figure 6 (for the Nord-South direction) and in Figure 7 (for the horizontal direction). The horizontal direction functions are obtained as the vector addition in the frequency domain of time histories in East-West and North-South directions.
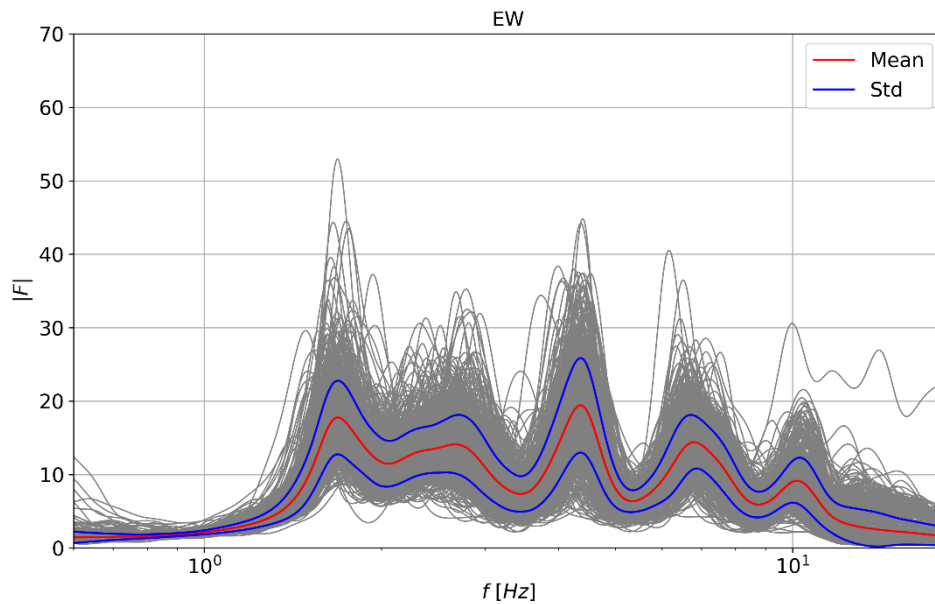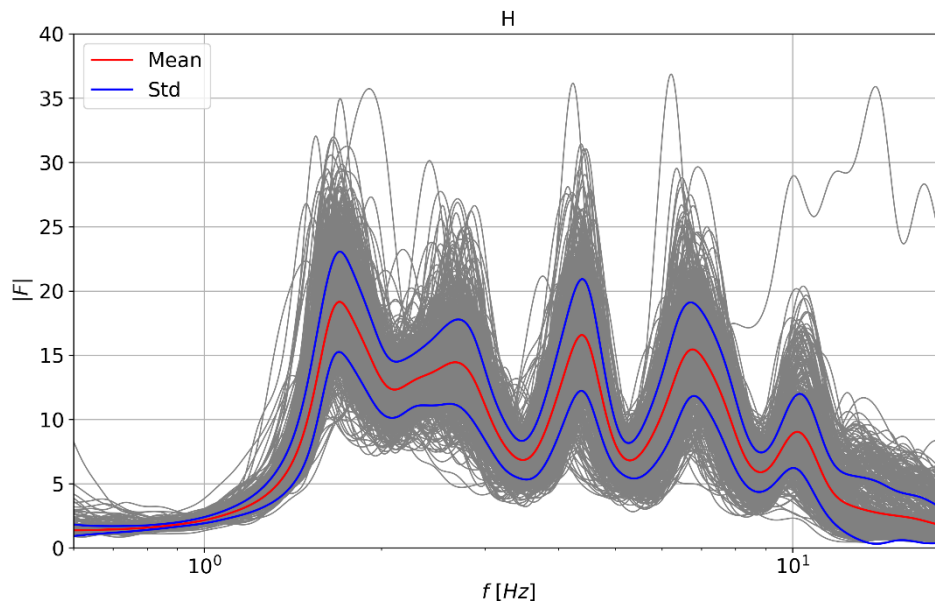
Figure 5: Transfer function trend for all time histories in direction East-West (EW) with mean (in red) and ± one standard deviation (in blue)
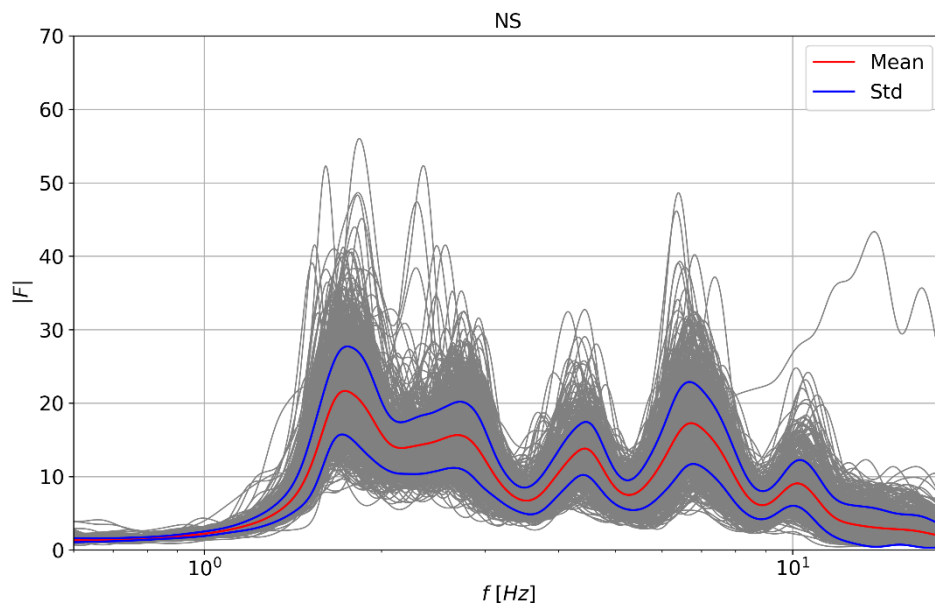
Figure 6: Transfer function trend for all time histories in direction Nord-South (NS) with mean (in red) and ± one standard deviation (in blue)

By observing the trend of the transfer functions in all directions, a large variability regarding main frequencies and amplitude peaks of the functions is shown. **The main objective of this work is to explain this variability. Kushiro10 site is considered to be a 1D vertical propagation site and nonlinear soil behavior cannot explain all of the variability encountered. The strong variability shown in Figure 3-5 is clearly not compatible with**

the linear 1D vertical propagating wave hypothesis. Indeed, the transfer function of a 1D elastic propagation site is unique and independent of the time histories. In the following analysis, the transfer functions related to horizontal direction will be considered as characteristic of a seismic event for this site rather than the East-West and North-South component.

Figure 7: Transfer function trend for all time histories in horizontal direction with mean (in red) and ± one standard deviation (in blue)

3. Qualitative sensitivity analysis of transfer functions for Kushiro10 site

In this chapter, a detailed analysis is done according to some fundamental parameters:

- The peak ground acceleration (PGA) of all time histories;
- The Azimuth between site and seismic source;
- The incidence angle of the seismic signal at the bedrock;
- The experimentally evaluated damping of the Kushiro10 soil column.

3.1. Input parameter Dataset

First of all, we provide some information regarding the localization of seismic inputs. Figure 8 and Figure 9 show the depth of the seismic sources and the epicentral distance of the seismic sources, respectively. Most of the seismic events are localized between 20 and 100 km of depth and below 300 km of epicentral distance from Kushiro10 site. The epicentral distance is calculated as follows (Stein & Wysession, 2005):

$$D_E = 2R_E\sqrt{[\sin(0.5[Lat_{sou} - Lat_{sta}])]^2 + \cos(Lat_{sou}) \cdot \cos(Lat_{sta}) \cdot [\sin(0.5[Lon_{sou} - Lon_{sta}])]^2} \qquad (3.1)$$

where:

- R_E is the Earth radius, estimated at 6370 km;
- Lat_{sou} and Lat_{sta} are, respectively, the latitude of seismic source and the latitude of seismic record station;
- Lon_{sou} and Lon_{sta} are, respectively, the longitude of seismic source and the longitude of seismic record station.
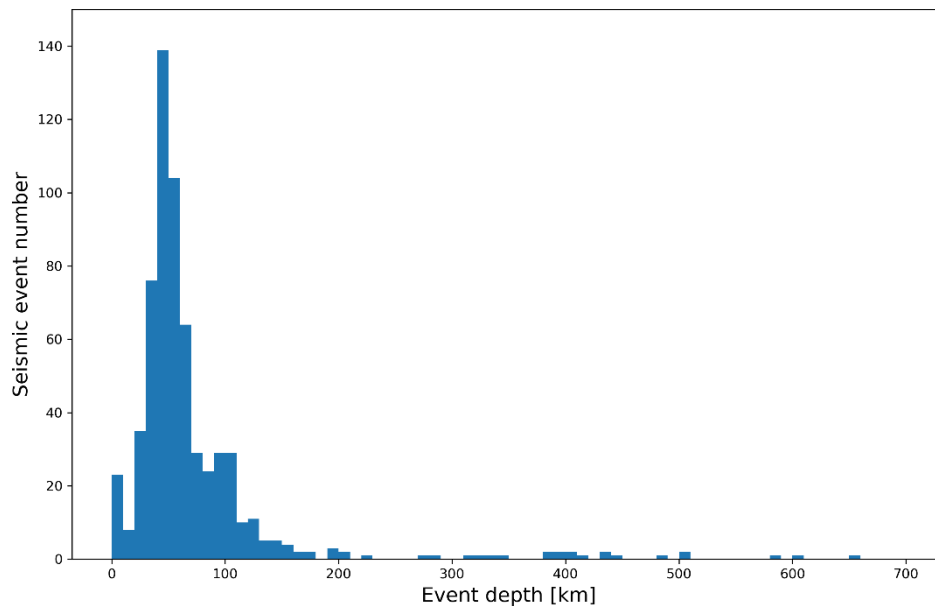

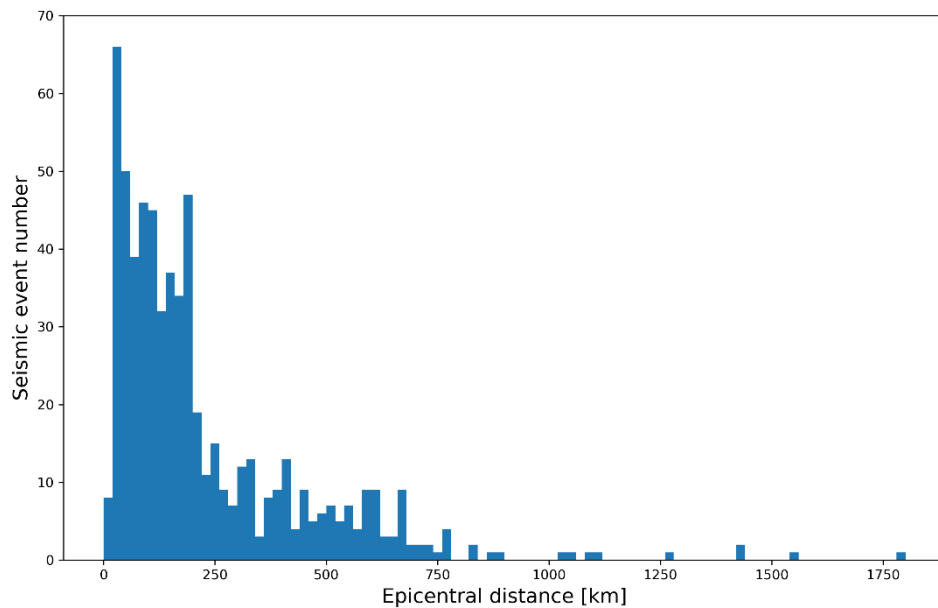**Figure 8: Distribution of the depth of the seismic sources**

Figure 9: Distribution of the epicentral distance of seismic sources

Furthermore, such analysis mix geometrical (due to the tectonic context of subduction) and attenuation effects that can affect the ray paths between the source and the two sensors. Nevertheless, the earthquakes used are mainly located 100 to 200km around the Kushiro10 site which is 10 times the distance between the surface sensor and the in-depth sensor that we use in this study (Figure 10). We thus consider - at first order - that waves have "a common" way between the two sensors, which implies that the variability we observe is due to "local" site effects.
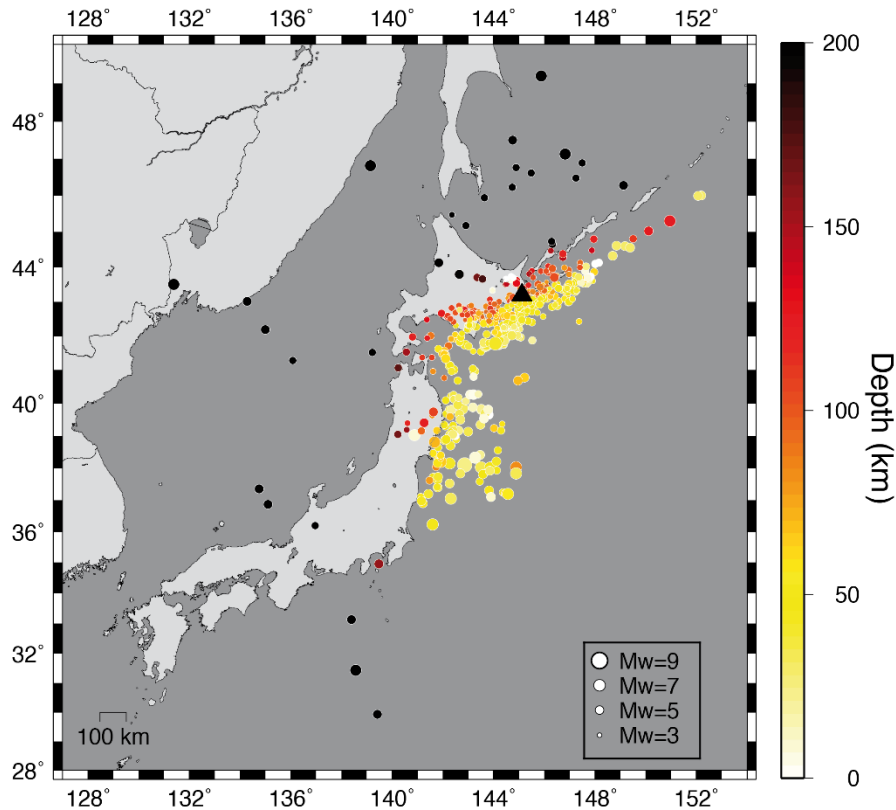
Figure 10 : Source depth of Kushiro10 signals

This strong assumption is also supported by the fact that attenuation properties over Japan have been particularly well carried out by numerous authors which have benefited from the high density of seismometers (and high seismicity) which cover the entire country. As an example, (Carcolé & Sato, 2010) have mapped the spatial variation of attenuation properties with a high amount of details by distinguishing elastic and anelastic processes. Thus, they allow to quantify the mean free path and the absorption length which are in the range 90-135km and 40-140km, respectively at national scale and for the central frequency 1Hz (minimum value) and 25Hz (maximum value). Such an analysis indicates that even if attenuation properties can affect the ray paths, considering our geometrical configuration with sensor and earthquake locations (large epicentral distance range compared to the distance between our two sensors) and the attenuation properties of Japan (large mean free path and absorption length compared to the distance between our two sensors), we are quite confident that, at least in the intermediate to high frequencies, the variability of the records are mainly due to local effect.

3.2. PGA Analysis

A first qualitative overview of PGA impact on RSR is given by plotting the transfer functions in increasing (Figure 11) and decreasing (Figure 12) order of PGA value.
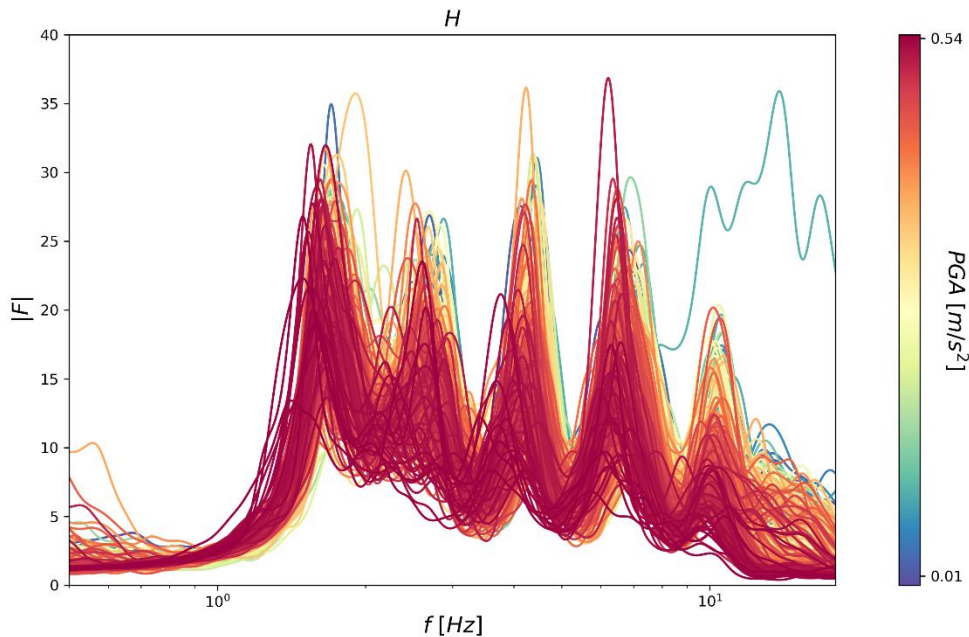
Figure 11: All transfer functions graphing by ascending order of PGA

As shown in Figure 12, for low values of PGA the trend of all transfer functions exhibit less dispersion. **In particular, the first eigenfrequency shows a higher value compared to the transfer functions on high values of PGA. This behavior confirms that the 1D linear propagation hypothesis for the Kushiro10 site is adequate for low values of PGA, when the non-linear effects are not activated due to the low intensity of seismic signal**. As shown in Figure 11, for high values of PGA the behavior of transfer functions is not uniform and is not in agreement with the 1D elastic propagation hypothesis for the Kushiro Site. With this analysis, it has been shown that the transfer functions are significantly impacted by the PGA values of each recorded time history. **In order to use the 1D elastic hypothesis propagation for Kushiro site, the high intensity seismic signals cannot be used to study the linear 1D response site**. In this analysis, we refer to the rock PGA (recorded at the deep sensor).
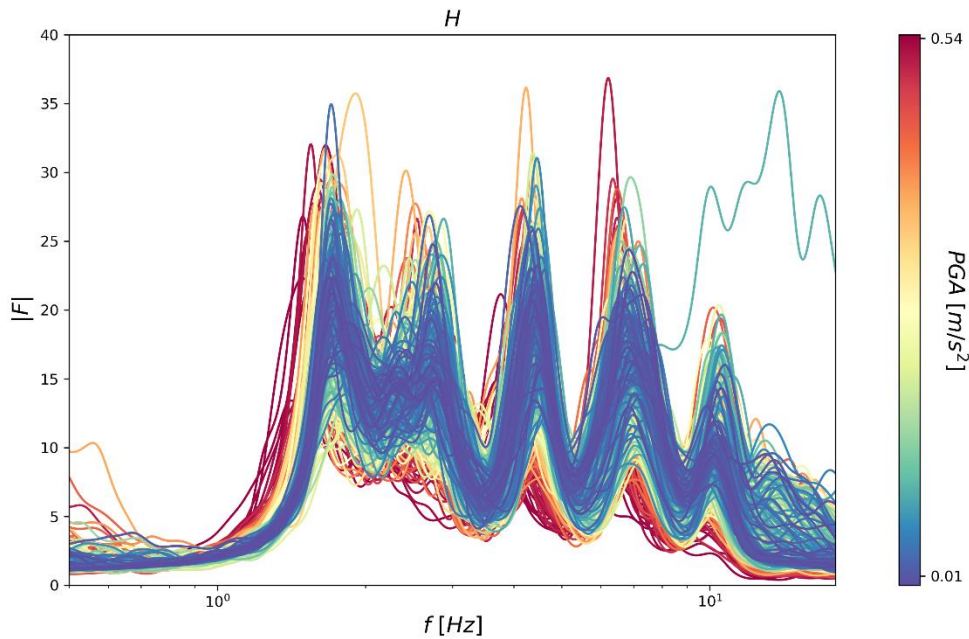
Figure 12: All transfer functions graphing by descending order of PGA

3.3. Azimuth Analysis

The second analysis is done by plotting all transfer functions according to the Azimuth value (Figure 13), calculated between site and seismic source.

The Azimuth value has been calculated as follows (Stein & Wysession, 2005):

$$x = \cos(lat_1) \cdot \sin(lat_2) - \sin(lat_1) \cdot \cos(lat_2) \cdot \cos(long_2 - long_1)$$
$$\sin(long_2 - long_1) \cdot \cos(lat_2)$$
$$Az(x, y) = 2 \cdot \text{atan} \frac{y}{\sqrt{x^2 + y^2} + x}$$

(3.2)

where:

- lat_1 and $long_1$ are the geographical coordinates of the seismic source;
- lat_2 and $long_2$ are the geographical coordinates of the record station;
- $Az(x, y)$ is the Azimuth between seismic source and record station, calculated by taking the geographical north pole as reference.

Figure 13, does not indicate any **(qualitative) correlation (or link) between the transfer functions and the Azimuth value**. This result is not surprising because: i) by calculating a spectral ratio, all regional propagation effects (so all energy directivity effects) have been released and ii) the whole time series have been considered, so the waves contained in the signal (not only direct waves) have mostly lost the information of their path by propagating from the crust to the borehole.
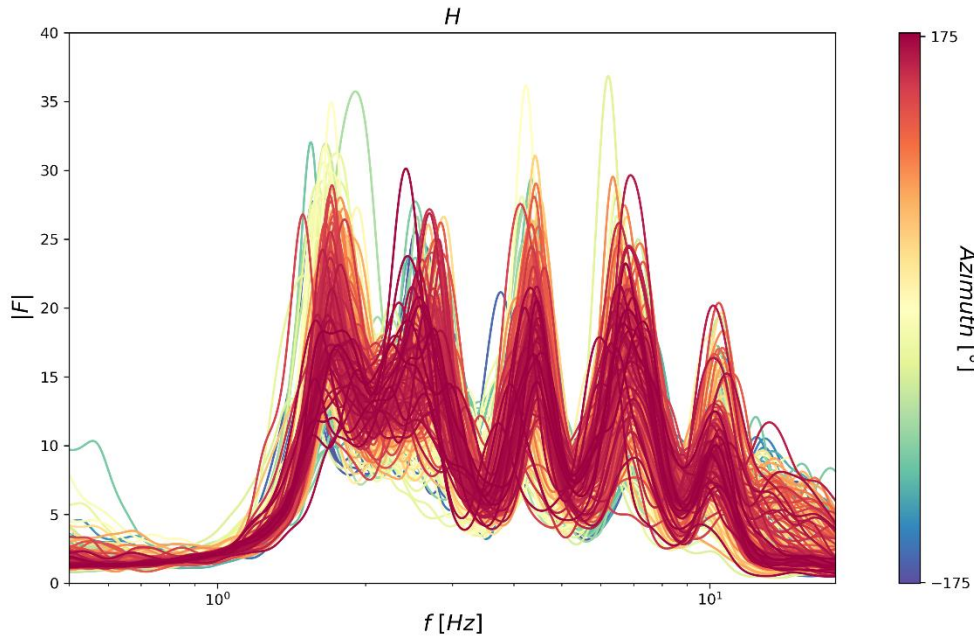
Figure 13: All transfer functions graphing according to the Azimuth value

3.4. Incidence angle analysis

In this section, the main interest is to compute the incidence angle of the seismic wave with the bedrock of the Kushiro10 soil column. In order to accomplish this, a theory for a spherical earth using the travel times of seismic waves is used. Here, few details are presented. For more details please refer to (Stein & Wysession, 2005).

3.4.1. Snell's law

Snell's law is a formula used to describe the relationship between the angles of incidence and refraction, when referring waves are passing through a boundary between two different isotropic media.

To describe the Snell's law, it is useful to define the apparent velocity, c_x, the velocity at which a plane wave appears to travel along a horizontal surface. We consider *P–SV* waves propagating in the *x–z* plane that are described by harmonic plane wave solutions of the scalar wave equations:

$$(P) \ \Phi(x,y,z,t) = A \cdot \exp(i(\omega t - k_x x \pm k_{z_\alpha} z)$$
$$(SV) \ \Psi(x,y,z,t) = B \cdot \exp(i(\omega t - k_x x \pm k_{z_\beta} z)$$

(3.3)

where:
- k is the wave vector;
- α is the propagation velocity of P-wave;
- β is the propagation velocity of S-wave;
- ω is the angular frequency of the wave.

The direction of wave propagation is described by the wave vector, which is the normal vector to the wave fronts. As shown in Figure 14, for a plane wave traveling in the x–z plane, the propagation direction is given by the wave vector (k_x, k_y) or the incidence angle, i, between the wave vector and the vertical. In a time increment Δt the wave front moves to a distance $v\Delta t$, where v is the medium velocity, and sweeps out a distance along the surface $c_x \Delta t$, where c_x is the apparent velocity along the surface (top figure). For a plane wave traveling vertically, the incidence angle $i = 0°$, k equals k_z, and c_x is infinite (middle figure). For a plane wave propagating horizontally, $i = 90°$, k equals k_x, and c_x equals the medium velocity (bottom figure). Thus, the horizontal wave velocity is:

$$c_x = \frac{v}{\sin i} \tag{3.4}$$

The apparent velocity is always greater than or equal to the medium velocity, α for P waves and β for S waves.
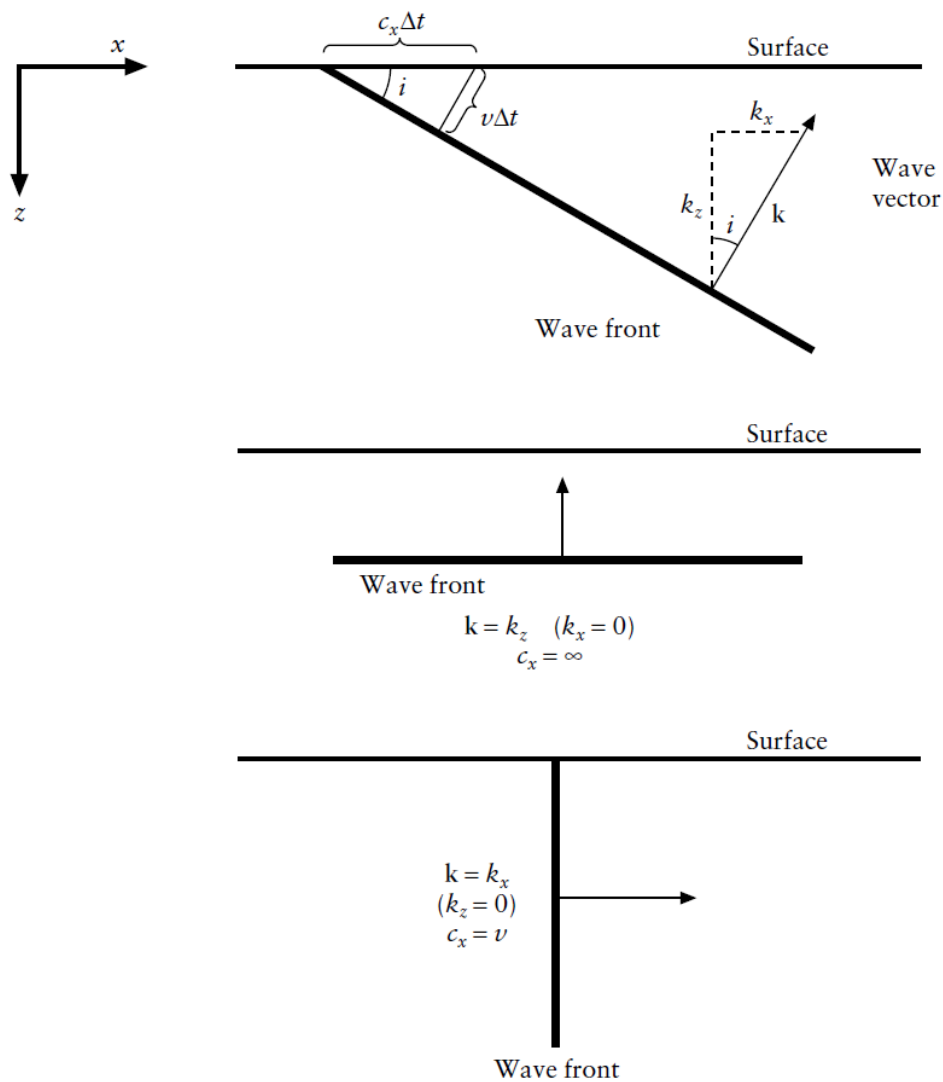

Figure 14: The wave vector, k, is normal to the wave front and points in the direction of propagation

Through a mathematical demonstration (that is detailed in (Stein & Wysession, 2005)) it is possible to show that the horizontal wavenumber k_x, and hence the apparent velocity c_x along the interface between two different materials, must be the same for each wave. This condition and the definition of c_x (Equation (3.4)) lead to the familiar form of **Snell's law**:

$$c_x = \frac{\alpha_1}{\sin i_1} = \frac{\beta_1}{\sin j_1} = \frac{\alpha_2}{\sin i_2} = \frac{\beta_2}{\sin j_2} \tag{3.5}$$

where (as shown in Figure 15 and Figure 16):
- α_1 and β_1 are, respectively, the velocity of P-wave and S-Wave of the top layer;
- α_2 and β_2 are, respectively, the velocity of P-wave and S-Wave of the top layer;
- i_1 is the incidence angle of incident/reflected P-wave;
- j_1 is the incidence angle of incident/reflected S-wave;
- i_2 is the incidence angle of transmitted P-wave;
- j_2 is the incidence angle of transmitted S-wave.
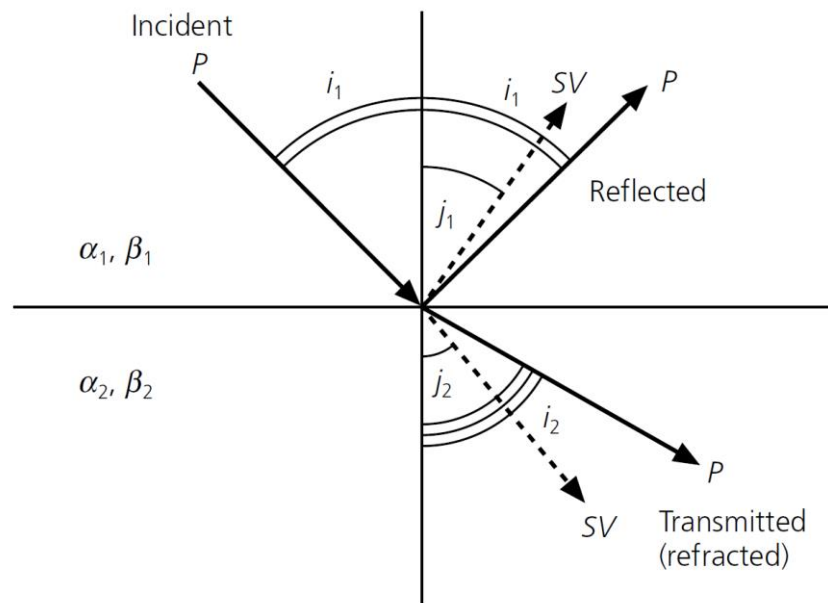

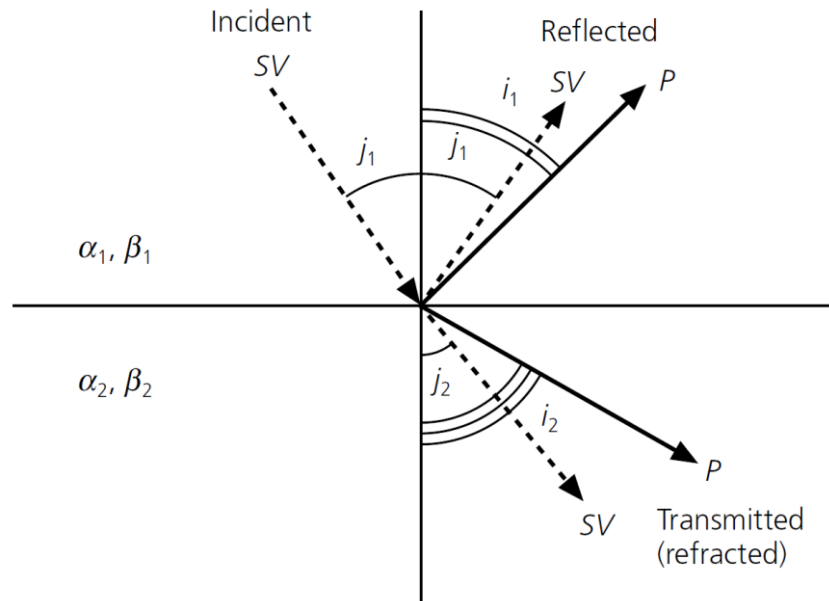**Figure 15: An incoming P-wave generates transmitted and reflected P and SV-waves**

Figure 16: An incoming S-wave generates transmitted and reflected P and SV-waves

3.4.2. Ray parameter

A useful way to characterize a wave's ray path is by considering its ray parameter, p, the reciprocal of the horizontal apparent velocity:

$$p = \frac{1}{c_x} = \frac{\sin i}{v} \tag{3.6}$$

where:

- i is the incidence angle of either P or an S-wave;
- v is the corresponding velocity.

3.4.3. Seismic wave in a spherical earth

In the previous sections, some elements have been given to study the velocity structure of a medium composed of flat layers. This analysis is useful when the epicentral distance is short enough to neglect the earth's curvature. Moreover, for greater distances and greater depths, a corresponding theory for a spherical earth can be obtained (Stein & Wysession, 2005).
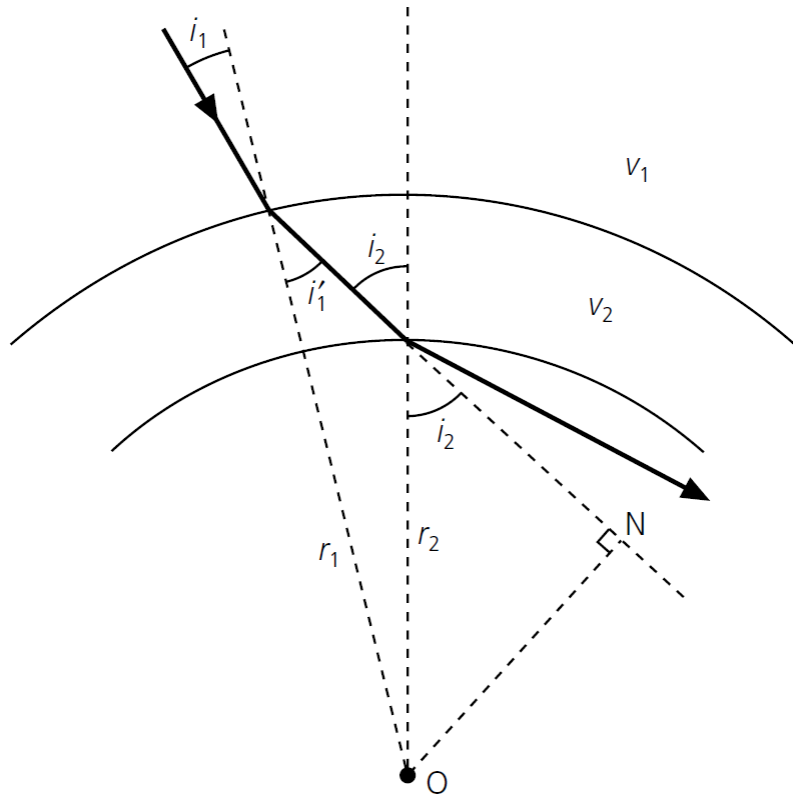
Figure 17: Geometry of Snell's law for a spherical earth

Let's consider the portion of a seismic ray's path connecting points at radial distances r_1 and r_2 from the earth's center (Figure 17). If v_1 and v_2 are the velocities above and below r_1, and i_1, i_1' and i_2 are the angles shown, then by Snell's law:

$$\frac{r_1 \sin i_1}{v_1} = \frac{r_1 \sin i_1'}{v_2} \tag{3.7}$$

However, $r_1 \sin i_1' = r_2 \sin i_2$ because both equal to the length $\overline{ON}$, so Equation (3.7) can be rewrite as follows:

$$\frac{r_1 \sin i_1}{v_1} = \frac{r_2 \sin i_2}{v_2} \tag{3.8}$$

Thus we define the ray parameter p for a spherical earth as:

$$p = r \cdot \frac{\sin i}{v} \tag{3.9}$$

where:

- r is the radial distance from the center of the Earth;
- v is the velocity at that point;
- i is the incidence angle between the ray path and the radius vector.

In literature, many time travel models exist. One of the most famous model, IASP91 (Kennett & Engdahl, 1991), has been used to compute the ray parameter for each wave:

- For the radial distance from the center of the Earth, $r = R_{Earth} - D_{wave}$ has been considered, where $R_{Earth} = 6371\ km$ approximately and D_{wave} is the depth of the seismic source, provided by KiK-net data;
- For the velocity at that point, $v = 3360\ m/s$ has been considered as approximation of SH-wave velocity in depth.

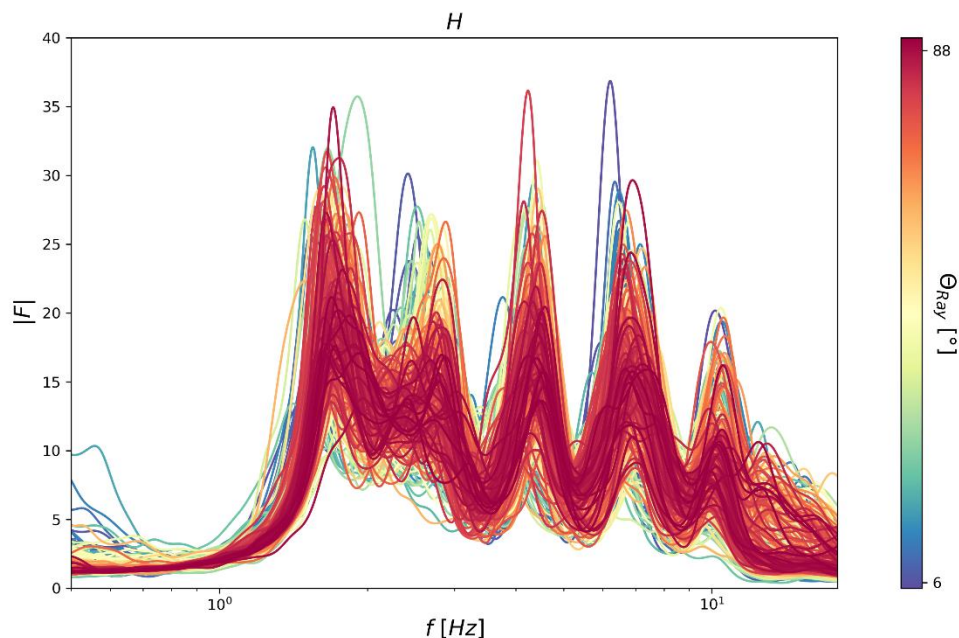By inversing the formula of ray parameter (Equation (3.9)), the incidence angle can be easily computed.

Figure 18: All transfer functions ordered by ascending order of incidence angle

As the analysis have been made on a SH vertical propagating wave model, only the sources producing SH waves propagating to the surface have been chosen (according to this model not all sources produce SH wave propagating to the surface; in this case, more of 90% of the sources produces SH wave propagating to the surface). Finally, all events not producing SH wave propagating to the surface have been excluded from this analysis.

As shown in Figure 18 and in Figure 19, qualitatively the transfer functions tend toward a more uniform shape if they are ordered by incidence angle. In particular, for low values of incidence angle, the 1D propagation hypothesis for Kushiro10 site seems to be obtained, because the seismic waves propagate in vertical direction, as it should be in this particular hypothesis. With this analysis, a second source of variability has been clearly identified. **In order to use the 1D elastic vertical propagation hypothesis for the Kushiro10 site, the seismic signals with a high value of incidence angle with the bedrock should be removed from the database to study the 1D response site**.
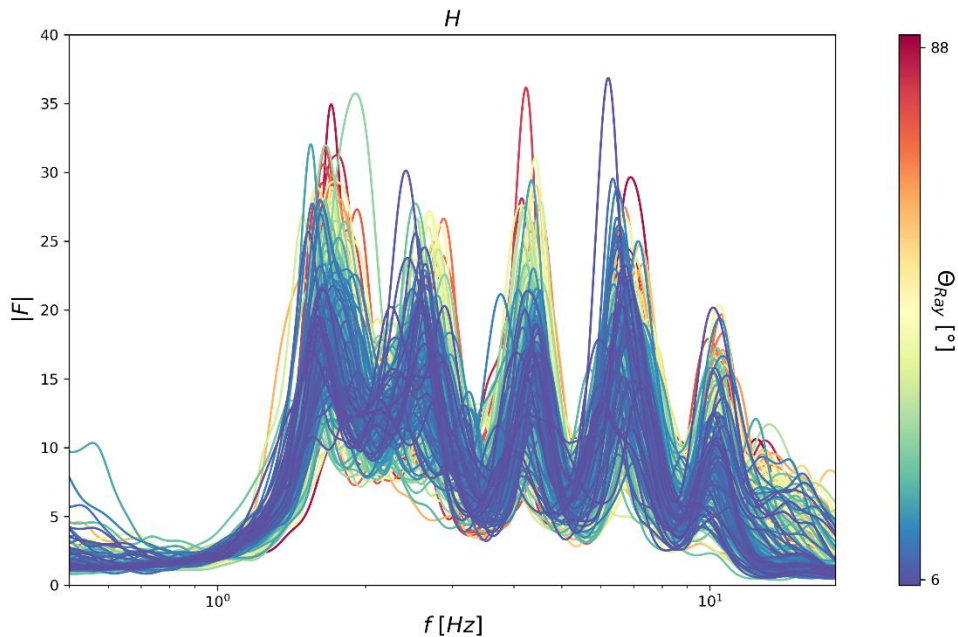
Figure 19: All transfer functions ordered by descending order of incidence angle

3.5. First summary of the variability sources

At this step of the study, a first summary of the variability sources analyzed can be made. In particular, all transfer functions have been filtered by two criteria:

- Only the transfer functions with an incidence angle $\Theta_{Ray} < 15°$ have been considered;
- Only the transfer functions with a $PGA < 0.15 \, m/s^2$ have been considered.

As shown in Figure 20 and Figure 21, the most impactful variability source is the incidence angle with bedrock. In the end, the filter on Θ_{Ray} and PGA has a positive effect on the dispersion of transfer functions. Indeed, with this filter, the standard deviation encloses almost the filtered transfer functions (Figure 22).

Standard deviation	f_1	f_2	f_3
All signals	3.89	3.78	4.34
Selected signals	1.75	4.01	2.46

Table 2 : Standard deviation computed on the first three eigen-frequencies

The standard deviation of the first three eigen-frequencies has been calculated and a comparison between the standard deviation calculated with all Fourier Spectra and selected Fourier Spectra has been made (Table 2). In particular, for the first and the third eigen-frequency, we can remark a significantly decreasing of the standard deviation.
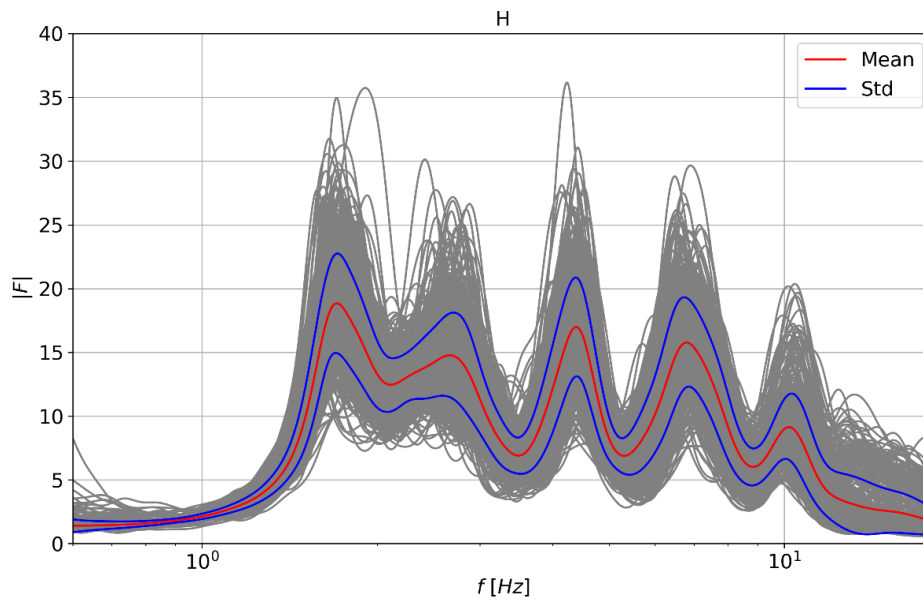
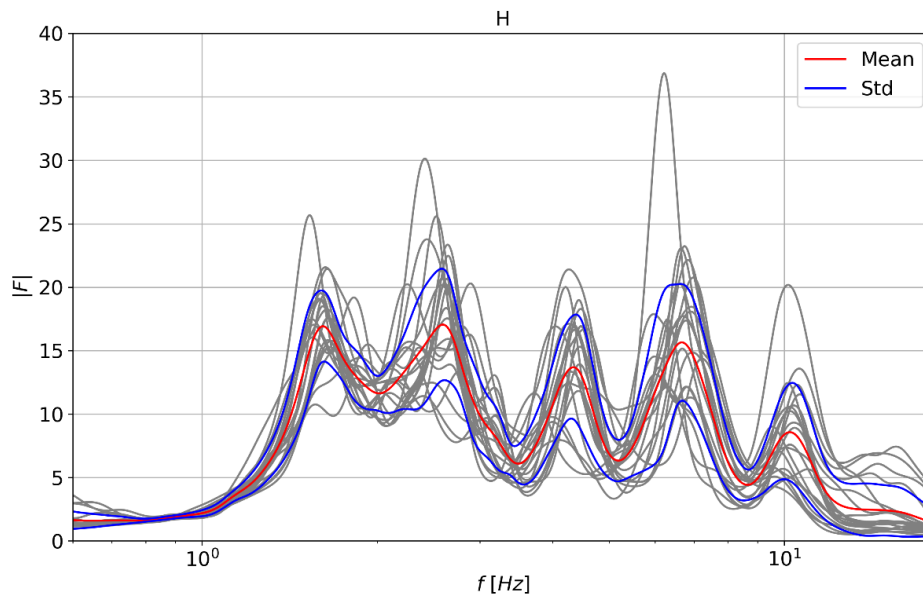**Figure 20: Transfer functions with a $PGA < 0.15\ m/s^2$ with std and mean of all TFs**

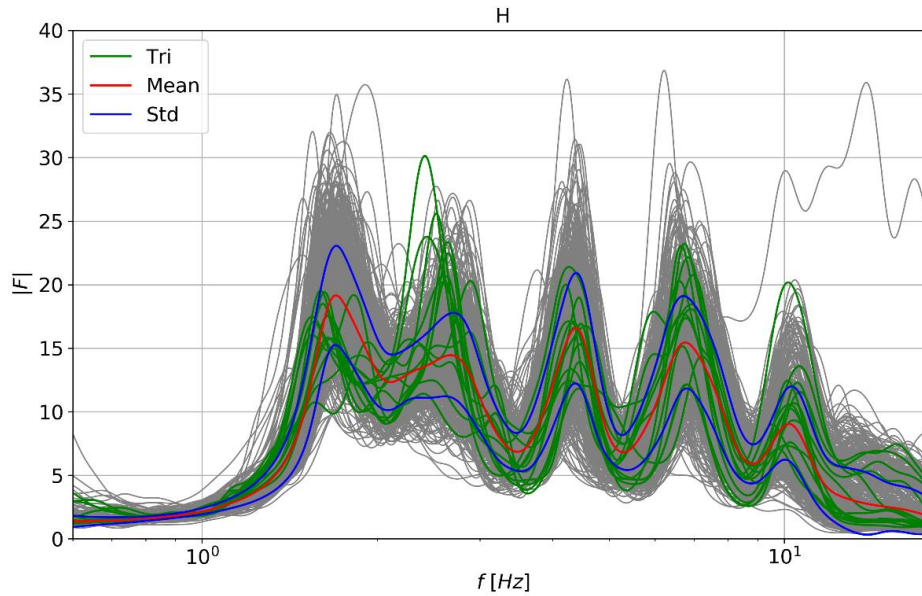**Figure 21: Transfer functions with $\Theta_{Ray} < 15°$ with std and mean of all TFs**

Figure 22: All transfer functions (gray) with their mean and standard deviation and the transfer functions with $\Theta_{Ray} < 15°$ and $PGA < 0.15 \, m/s^2$ (green)

3.6. Damping analysis

The main objective of the damping analysis is to evaluate the elastic attenuation in order to compare the values obtained from the damping model explained in the following paragraphs with the experimental values (Table 1). To this purpose, a methodology highly consolidated in literature is applied. In the next paragraph, the main concepts will be presented.

3.6.1. Background

It is well known in seismology theory that the amplitude of seismic waves decreases during their travel in Earth's crust. It has long been recognized that the amplitude of direct S-wave filtered in a narrow frequency-band can be approximated by an equation of the following form (Futterman, 1962):

$$A(r, f) = A_0 \exp(-\pi f r / Q_{ef} V_s) \tag{3.10}$$

where:

- r is the distance;
- f is the frequency;
- Q_{ef} is the effective seismic quality factor of S-waves which quantified the direct S-wave seismic attenuation through Q_{ef}^{-1} ((Lay & Wallace, 1995), (Sato, et al., 2002) or Sato et al., 2002 for details)
- V_s is the S-wave velocity of the medium

After studying the high-frequency decay of accelerograms recorder in California, (Anderson & Hough, 1984) suggested that the shape of the S-wave acceleration spectrum at high frequencies could be described by an equation similar to (Cormier, 1982) that they define as follows:

$$A(f) = A_0 \exp(-\pi k f) \qquad f > f_E \tag{3.11}$$

where:

- The amplitude A_0 depends on factors such as source properties and propagation distance;
- k is a spectral decay parameter;
- f_E is a frequency beyond which the slope of the spectrum is approximately linear on a plot of the logarithm of $A(f)$ versus f.

Usually, the attenuation parameter can be written as $k = k_0 + k_r \cdot R$, where k_0 is the site attenuation parameter, k_r is the regional attenuation parameter and R is the epicentral distance. Adopting the (Hough & Anderson, 1988) relationship and using notation from (Campbell, 2009), the site attenuation parameter (k_0) can be computed as follows:

$$k_0 = k_0^{rock} + \int_0^z Q_{ef}(z)^{-1} V_s(z)^{-1} dz \tag{3.12}$$

where k_0^{rock} is the attenuation parameter for the bedrock. The value of Q_{ef} can be readily converted to soil damping (at low deformation) as follows:

$$D_{min}(\%) = \frac{100}{2Q_{ef}} \tag{3.13}$$

The Equation (3.12) can be rewritten as follows:

$$k_0 = k_0^{rock} + \int_0^z \frac{2D_{min}}{100} V_s(z)^{-1} dz \tag{3.14}$$

3.6.2. Attenuation parameter on Kushiro site

As the accelerograms of the Kushiro site are available on two distinct points (borehole and surface) and the soil column characteristics are also available, it is possible to determine the site kappa by:

- Computing the attenuation parameter on the borehole and surface accelerograms. For this purpose, the k parameter is calculated as the slope of the Fourier spectrum on logarithmic scale between 20 Hz and 40 Hz
- Computing the site kappa as the difference of the attenuation parameter (Δk) between borehole and surface;
- Comparing this difference $k_0 - k_0^{rock}$ with the value of $\alpha = \int_0^z \frac{2D_{min}}{100} V_s(z)^{-1} dz$.

In Figure 23 and in Figure 24, borehole and surface Fourier spectra in logarithmic scale are shown. In Figure 25, the value of Δk computed on the accelerograms for each seismic signal is shown. The α value is equal to 0.69. So, the ratio $\Delta k/\alpha$ gives information about the difference between the attenuation parameter obtained through the borehole and surface accelerograms

and the attenuation parameter obtained through the soil column characteristics (with the Equation (3.14)). By taking into account all the single values, a clear trend cannot be observed, because a very large variability is shown. The majority of seismic signals provide a ratio $\Delta k/\alpha > 1$, so for these accelerograms the laboratory attenuation parameter seems to be underestimated. Few seismic signals provide a ratio $\Delta k/\alpha < 1$, so for these accelerograms the laboratory attenuation parameter seems to be overestimated.
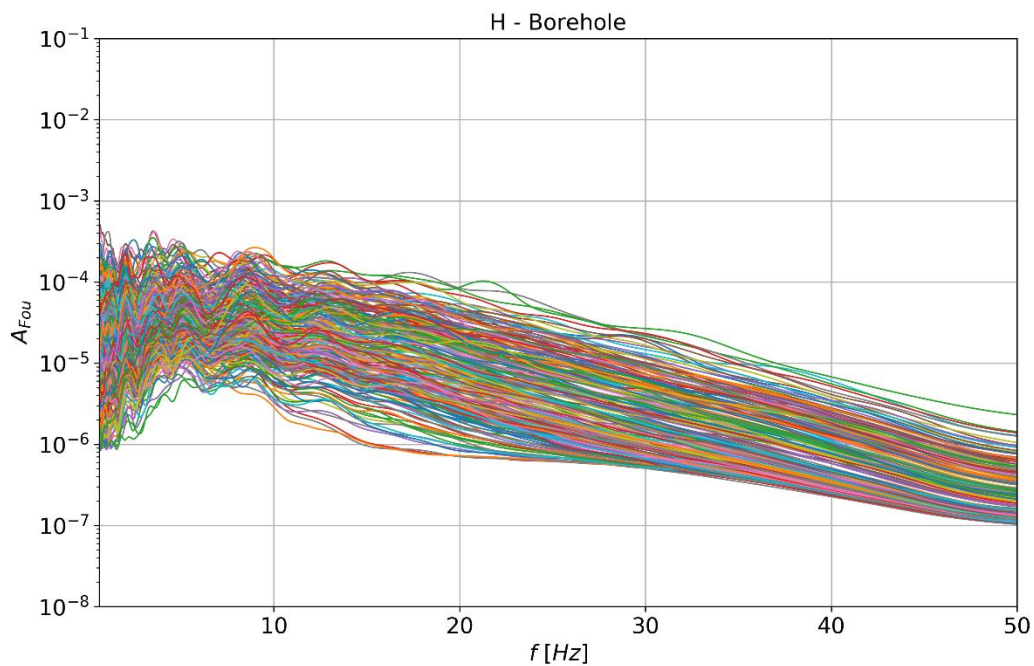

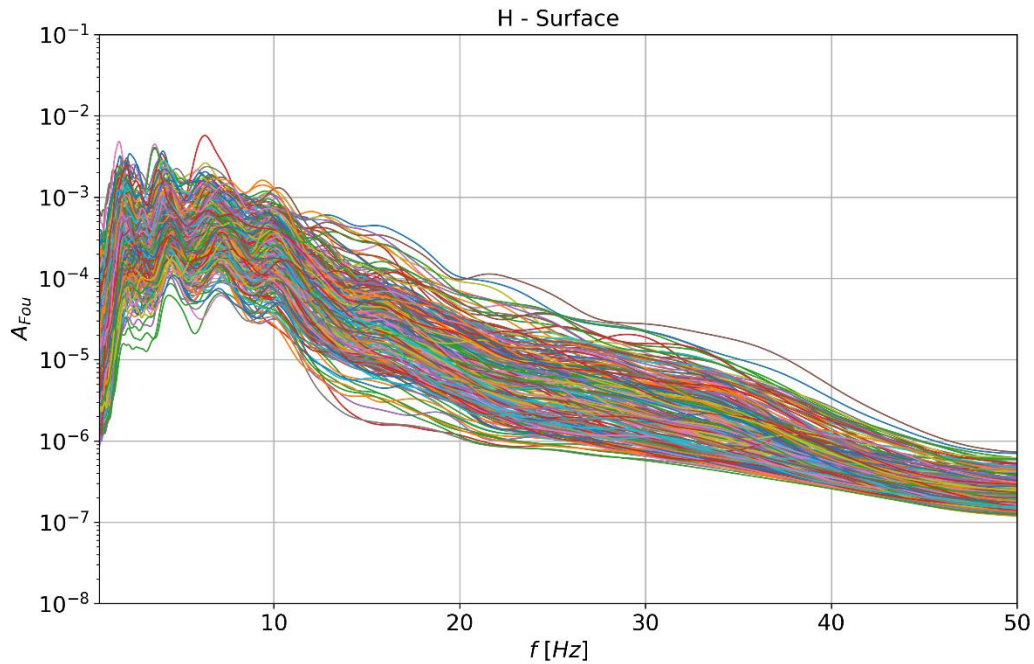**Figure 23: Borehole Fourier spectra in logarithmic scale**

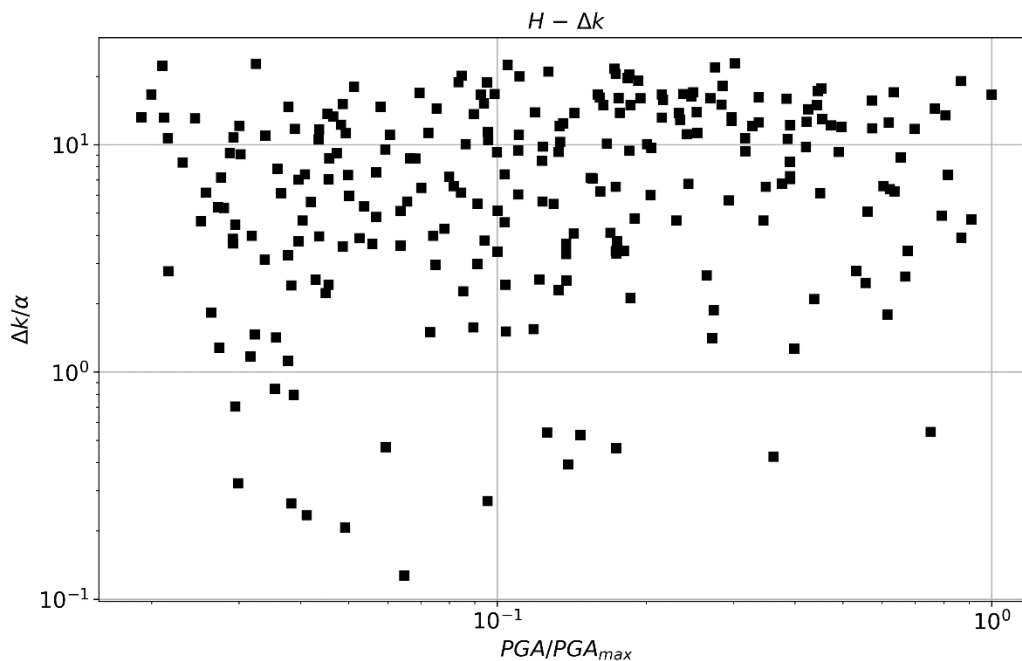**Figure 24: Surface Fourier spectra in logarithmic scale**

Figure 25: Value of Δk for each seismic signal in log scale

In Figure 26 and in Figure 27, the distribution of borehole and surface k with mean and standard deviation are shown, exclusively for the seismic signals with $PGA < 0.15\,m/s^2$. By taking the mean values of borehole and surface k, the ratio $\Delta k/\alpha$ can be calculated and it is equal to 3.6. **It means that the experimental elastic attenuation (Table 1) is underestimated by 3.6 times compared to the elastic attenuation obtained through the**

borehole and surface accelerograms. This result regarding the damping at low deformation is indicative about the underestimation of the elastic attenuation. Indeed, a real debate (Ktenidou, et al., 2014) exists around the k parameter in the scientific community. Apparently, the frequency band used to compute the k parameter is not the same for all signals, as shown by (Aki, 1980) and k is frequency-dependent. So, the interpretation of these results have to be made in a very carefully way and deserves to be better explored.
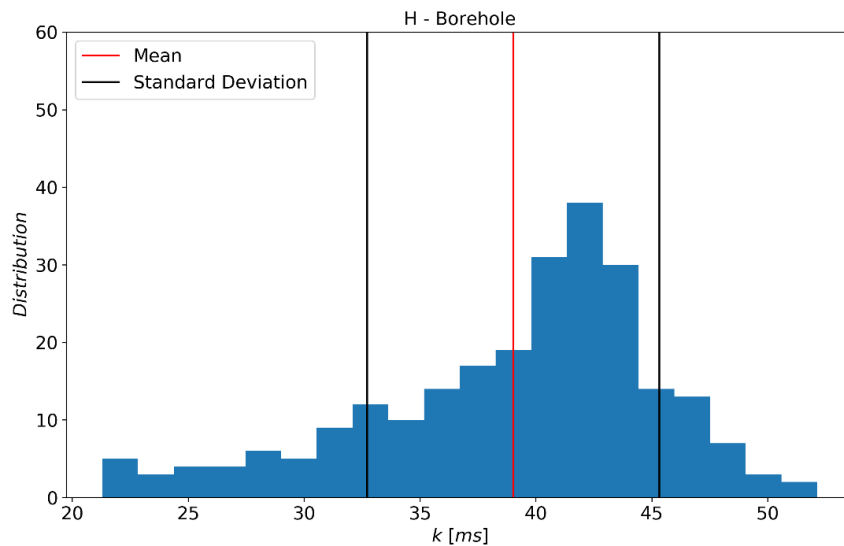

Figure 26: Distribution of borehole k with mean and standard deviation
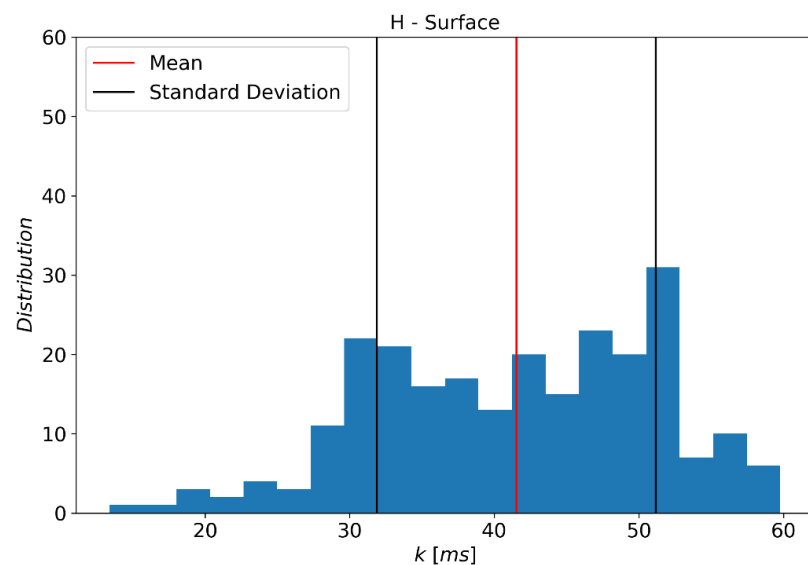

Figure 27: Distribution of surface k with mean and standard deviation

In this damping analysis, a possible discrepancy between the experimental laboratory damping and the damping that can be inferred from the records has been remarked. We did not furnish a definitive conclusion, as the results on the kappa analysis is today very controversial in the scientific community and our work is still ongoing. Also, we think that it would be interesting to further analyze this discrepancy with a 2D model, where we can consider a horizontal variability

on the damping parameter (not only) to see if we obtain the same variability on the NTF (Numerical Transfer Function obtained with the 2D model).

4.   Conclusions and perspectives

In this work, a qualitative analysis of the Kushiro10 site KiK-net data has been accomplished. This analysis has allowed to understand the main variability sources in transfer functions when considering the 1D vertical propagation site hypothesis. As for many KiK-net sites (Thompson, et al., 2012), the transfer functions of all time histories show a large variability in terms of eigen-frequencies and amplitudes. With the data analysis, two main variability sources have been identified:

1) The incidence angle that has a strong impact on the variability of the transfer functions;
2) The PGA values that have a medium impact on the variability of the transfer functions.

Also, an analysis of the damping has been made and it shows that the elastic attenuation could be underestimated. Therefore, other reasons should be investigated to explain the discrepancy. For instance other possible explanations have been proposed in (Pecker, 1995). This result deserves to be further investigated in the future.

These results suggest that the 1D propagation hypothesis is maybe too strong for the Kushiro10 site. Indeed, even if the site morphology suggests a 1D stratigraphy, a 1D site response model seems to be not enhanced enough to take into account the variability provided by the seismic signals (in particular the incidence angle) and by the damping.

Furthermore, in a future analysis, it would be highly interesting to repeat this kind of analysis for other sites and compare the results to Kushiro. The Figure 28 from (Thompson, et al., 2012) provides a comparison of σ_i (inter-event variability) for the different sites considered. The Kushiro10 site being a LG site, its variability is in the lower range (up to 0.35), while other sites can present larger values (up to 0.6).

In perspective, a 2D model can be considered to complete this study in order to further investigate these first results in terms of variability. A comparison between the 1D site response and the 2D site response could be a good method to test the impact of the incidence angle on the site response. Also, with a 2D model, a horizontal variability (El Haber, 2019) can be added in order to better explore the mechanical parameter variability (in particular the elastic attenuation that seems underestimated in a 1D model).
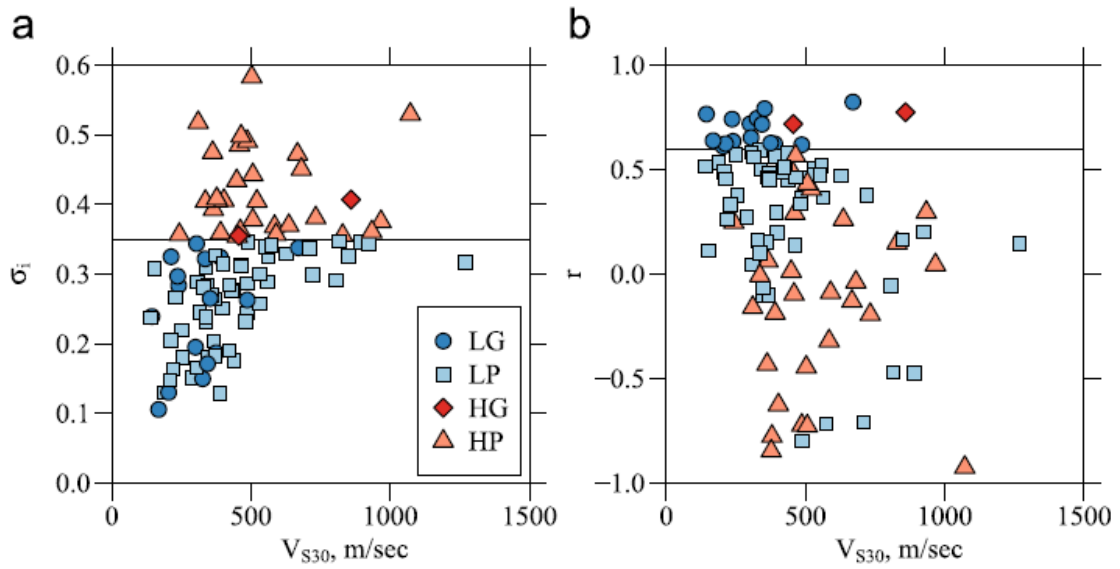
Figure 28 : Inter-event variability (a) and fit to SH1D site response model (b) for different japan sites

5. Bibliography

Aki, K., 1980. Scattering and attenuation of shear waves in the lithosphere. *Journal of Geophysical Research.*

Amorosi, A., Boldini, D. & di Lernia, A., 2016. Seismic ground response at Lotung: Hysteretic elasto-plastic-based 3D analyses. *Soil Dynam. Earthq. Eng.,* Volume 85, pp. 46-61.

Anderson, J. G. & Hough, S. E., 1984. A model for the shape of the Fourier amplitude spectrum of acceleration at high frequencies. *Bull. Seismol. Soc. Am.,* Issue 74, p. 1969–1993.

Bonilla, L. F., Archuleta, R. J. & Lavallée, D., 2005. Hysteretic and dilatant behavior of cohesionless soils and their effects on nonlinear site response: Field data observations and modeling. *Bull. Seismol. Soc. Am.,* Volume 95, p. 2373–2395.

Campbell, K. W., 2009. Estimates of shear-wave Q and κ0 for unconsolidated and semiconsolidated sediments in Eastern North America. *Bull. Seismol. Soc. Am.,* Issue 99, pp. 2365-2392.

Carcolé, E. & Sato, H., 2010. Spatial distribution of scattering loss and intrinsic absorption of short-period S waves in the lithosphere of Japan on the basis of the Multiple Lapse TimeWindow Analysis of Hi-net data. *Geophysical Journal International,* pp. 268-290.

Cormier, V. F., 1982. The effect of attenuation on seismic body waves. *Bull. Seismol. Soc. Am.,* Issue 72, p. 169–S200.

El Haber, E., 2019. *Effet de la variabilité spatiale des propriétés du sol sur la variabilité de la réponse sismique,* s.l.: Phd.

Elgamal, A.-W., Zeghal, M., Tang, H. T. & Stepp, J. C., 1995. Lotung downhole array. I: Evaluation of site dynamic properties. *J. Geotech. Eng.,* Volume 121, pp. 350-362.

Futterman, W. I., 1962. Dispersive body waves. *J. Geophys,* Issue 67, p. 5279–5291.

Gunturi, V. R., Elgamal, A.-W. & Tang, H. T., 1998. Hualien seismic downhole data analysis. *Eng. Geol.,* Volume 50, p. 9–29.

Hough, S. E. & Anderson, J. G., 1988. High-frequency spectra observed at Anza, California: Implications of Q structure. *Bull. Seismol. Soc. Am.,* Issue 78, pp. 692-707.

Ishibashi, I. & Zhang, X., 1993. Unified dynamic shear moduli and damping ratio of sand and clay. *Soils Found.,* Volume 33, pp. 182-191.

Kennett, B. L. N. & Engdahl, E. R., 1991. Traveltimes for global earthquake location and phase identification. *Geophysical Journal International,* 2(105), pp. 429-465.

Konno, K. & Ohmachi, T., 1998. Ground-Motion Characteristics Estimated from Spectral Ratio between Horizontal and Vertical Components of Microtremor. *Bulletin of the Seismological Society of America,* 88(1), pp. 228-241.

Kramer, S. L., 1996. *Geotechnical Earthquake Engineering.* s.l.:William J. Hall.

Ktenidou, O.-J., Cotton, F., Abrahamson, N. A. & Anderson, J. G., 2014. Taxonomy of: A Review of Definitions and Estimation Approaches Targeted to Applications. *Seismological Research Letters,* 85(1), pp. 135-148.

Lay, T. & Wallace, T., 1995. *Modern Global Seismology.* San Diego, California: Academic.

NIED, 2019. *Strong-motion Seismograph Networks (K-NET, KiK-net).* [Online] Available at: http://www.kyoshin.bosai.go.jp/

Olsen, K. S., Day, S. & Bradley, C., 2003. Estimation of Q for long-period (> 2 sec) waves in the Los Angeles basin. *Bull. Seismol. Soc. Am.,* Volume 93, p. 627–638.

Pecker, A., 1995. Validation of small strain properties from recorded weak seismic motions. *Soil Dynamics and Earthquake Engineering,* Issue 14, pp. 399-408.

Regnier, J., 2013. *Variabilité de la réponse sismique : de la classification des sites au comportement non-linéaire des sols,* École doctorale Sciences, Ingénierie et Environnement: Phd.

Régnier, J., Bonilla, L.-F. & Bard, P.-Y., 2018. PRENOLIN: International Benchmark on 1D Nonlinear Site-Response Analysis - Validation Phase Exercise. *Bulletin of the Seismological Society of America.*

Régnier, J., Bonilla, L. F., Bertrand, E. & Semblat, J. F., 2014. Influence of the Vs profiles beyond 30 m depth on linear site effects: Assessment from the KiK-net data. *Bull. Seismol. Soc. Am.,* Volume 104, p. 2337–2348.

Sato, H., Fehler, M. & Wu, R. S., 2002. Scattering and attenuation of seismic waves in the lithosphere. *International Handbook of Earthquake & Engineering Seismology.*

Seed, H. & Idriss, I. M., 1969. Influence of soil conditions on ground motions during earthquakes. *J. Soil Mech. Found,* 95(1), pp. 99-138.

Stein, S. & Wysession, M., 2005. *An Introduction to Seismology, Earthquakes, and Earth Structure.* s.l.:Blackwell Publishing.

Susilo, G. E., Yamamoto, K. & Imai, T., 2012. Modeling the groundwater fluctuation in Sphagnum mire in northern Hokkaido, Japan. *Environmental Sciences 8 (201,* Issue 13, p. 606 – 620.

Thompson, E. M., Baise, L. G., Tanaka, Y. & Kayen, R. E., 2012. A taxonomy of site response complexity. *Soil Dynamics and Earthquake Engineering,* Volume 41, pp. 32-43.

Vucetic, M. & Dobry, R., 1988. Cyclic triaxial strain-controlled testing of liquefiable sands. *Advanced Triaxial Testing of Soil and Rock.*

Yu, G., Anderson, J. G. & Siddharthan, R., 1993. On the characteristics of nonlinear soil response. *Bull. Seismol. Soc. Am.,* Volume 83, p. 218–244.

Zeghal, M., Elgamal, H. T., Tang, H. T. & Srepp, J. C., 1995. Lotung downhole array. II: Evaluation of soil nonlinear properties. *J. Geotech. Eng.,* Volume 121, p. 363–378.

Zhang, Z.-M., Chen, S. & Liang, Y.-Z., 2010. Baseline correction using adaptive iteratively reweighted penalized least squares. *The Royal Society of Chemistry,* Volume 135, p. 1138–1146.